Correspondence to:

H. Turner,
h.m.turner@reading.ac.uk

Using Solar Wind Data Assimilation Results to Drive Dynamic Solar Wind Models

Harriet Turner[1] , Mathew Owens[1] , Luke Barnard[1] , Matthew Lang[2], Edmund Henley[3] , François-Xavier Bocquet[3], Siegfried Gonzi[3] , C. Nick Arge[4], Rhiannon Biddiscombe[1] , and Tinatin Baratashvili[5]

[1]Department of Meteorology, University of Reading, Reading, UK, [2]British Antarctic Survey, Cambridge, UK, [3]Met Office, Devon, UK, [4]NASA GSFC, Greenbelt, MD, USA, [5]KU Leuven, Leuven, Belgium

Abstract A coupled modeling framework is often used to forecast the near-Earth solar wind conditions. This consists of a coronal model for close to the Sun and a heliospheric model for propagating the solar wind out to Earth. The coronal model is initialized using photospheric magnetic field observations and beyond this, there are no further observational constraints. Models are therefore essentially free-running, and so large errors can propagate through the model, reducing the accuracy of forecasts. Data assimilation is a technique that combines model output with observations to form an optimum estimation of reality. In the context of space weather forecasting, we can assimilate observations from orbiting spacecraft, which can be used to adjust the inner boundary of the heliospheric model. Previous work using solar wind data assimilation has made use of the Magnetohydrodynamics Around a Sphere (MAS) coronal model; however, the Wang-Sheeley-Arge (WSA) model is more commonly used operationally. In this work, we present how the Burger Radius Variational Data Assimilation (BRaVDA) scheme can be used with the WSA model to produce an updated inner boundary condition for the Heliospheric Upwind Extrapolation with time-dependence (HUXt) model. This involves processing the BRaVDA output, as this would be required for use in any solar wind model, and how the output can be used to modify the WSA map for use in 3D physics-based models. We find that BRaVDA can help with WSA bias correction and show that using the optimum level of processing can lead to improved solar wind forecasts.

Plain Language Summary Knowledge of the background solar wind conditions is necessary for accurate space weather forecasting, to mitigate against unwanted impacts. Current solar wind forecasting uses two models, one model for the region close to the Sun (coronal model) which feeds into a model for the solar system (heliospheric model). This process does not make use of observations to constrain forecasts, meaning that large errors can propagate through the forecasting models. Data assimilation (DA) combines observations with model output, forming an optimum estimation of reality. Here, we use a solar wind DA scheme to update the output from the coronal model to improve the forecasts produced by the heliospheric model. This is applied to the Wang-Sheeley-Arge (WSA) coronal model, which is widely used operationally for space weather forecasting. It is found that using DA improves the solar wind forecast performance over 2020 when using a simplified heliospheric model, and it can correct biases in the forecast. The optimum level of processing of the DA output is also found, as this is required for use with any heliospheric model. It is also shown how to use the DA output with more complex models, which are used operationally for space weather forecasting.

1. Introduction

Space weather has the potential to cause unwanted impacts such as GPS errors, damage to spacecraft and harming the health of astronauts and people on high-altitude flights (Cannon, 2013). Accurate space weather forecasting can potentially help mitigate these impacts; for example, Oughton et al. (2019) show potential impacts to the UK from a Carrington-sized 1-in-100 years event may be reduced from £2.9 billion (with current forecasting capabilities) to £0.9 billion (with enhanced forecast capabilities) and Eastwood et al. (2018) perform a similar analysis for European power grids. The most severe space weather is driven by the arrival of coronal mass ejections (CMEs) in near-Earth space (Gosling, 1993). However, accurate reconstruction of the ambient solar wind is still critical for space weather forecasting for two reasons. Firstly, CMEs must propagate through the solar wind, meaning ambient conditions can affect the CME's speed and arrival time at Earth (Case et al., 2008). Secondly, ambient solar wind can form stream interaction regions (SIRs), when fast solar wind catches up with slower solar

Space Weather

Luke Barnard, Matthew Lang, Edmund Henley, François-Xavier Bocquet, Siegfried Gonzi, C. Nick Arge, Rhiannon Biddiscombe, Tinatin Baratashvili

wind, leading to regions of higher density and magnetic field (Pizzo, 1982). SIRs are sources of recurrent space weather (Richardson & Cane, 2012); these are typically less impactful than the transient CMEs, but non-extreme space weather conditions can have economic impacts, and more common disturbances also merit attention (Guhathakurta, 2021; Schrijver, 2015; Schrijver et al., 2014).

A common approach for forecasting near-Earth solar wind conditions consists of a coupled modeling system between a coronal model (initialized with photospheric magnetograms) and a heliospheric model (e.g., Kieokaew et al., 2024; Pomoell & Poedts, 2018; Shiota et al., 2014). Typically, the coronal model covers the region from 1 to between 20 and 30 solar radii (rS) and is initialized with observations of the photospheric magnetic field. The Wang-Sheeley-Arge (WSA) model is a commonly-used coronal model in operational forecasting, due to computational efficiency and long-term tuning/testing against near-Earth observations (C. N. Arge et al., 2003). Beyond the coronal domain, the solar wind is modeled using a heliospheric model. This can be a very simple model, such as a ballistic propagation (e.g., Opitz et al., 2009; Timar et al., 2024), a reduced-physics model such as HUXt (used in this study, see Section 2.3; M. Owens, Lang, Barnard, et al., 2020), or the numerical solution to the full set of magnetohydrodynamic (MHD) equations, such as Enlil (Odstrcil, 2003). The coupled WSA-Enlil-Cone modeling system is a commonly implemented modeling framework (Kay et al., 2024; Riley et al., 2018) and is used operationally at the UK Met Office Space Weather Operations Center (MOSWOC) and at the US National Oceanic and Atmospheric Administration's Space Weather Prediction Center (NOAA SWPC).

Beyond the observations of the photospheric magnetic field, there are no further observational constraints on current operational near-Earth forecasts of the ambient solar wind. Some potentially-relevant observations able to provide such constraints are available, such as heliospheric images (e.g., Harrison et al., 2017); in situ L1 observations (e.g., Lang et al., 2021; Lang & Owens, 2019); or remote-sensing interplanetary scintillation observations (e.g., Jackson et al., 2023), but no operational systems yet integrate these. This means that the models are essentially free-running, and so large errors can propagate through the model, reducing the accuracy of forecasts. Data assimilation (DA) is a technique that combines model output with observations to form an optimum estimation of reality. It has been used in terrestrial weather forecasting and has led to large forecast improvements (Bauer et al., 2015; Kalnay, 2003); however, it has been underused in space weather forecasting. The Burger Radius Variational Data Assimilation (BRaVDA) scheme developed in Lang and Owens (2019) makes use of in situ solar wind observations close to Earth's orbital latitude and heliocentric distance to update the inner boundary of a heliospheric model, providing an improved solar wind state. The BRaVDA methodology is described further in Section 2.2.

Previous work on the use of DA in solar wind modeling has used near-Sun solar wind conditions estimated by the Magnetohydrodynamics Around a Sphere (MAS) coronal model, due to its large historical archive and availability (Turner et al., 2022, 2023). Due to the extensive use of the WSA model in operational space weather forecasting, this study investigates the use of WSA boundary conditions in the BRaVDA scheme and how the DA output can be processed for use in any solar wind model. The methodology, including model description and details of the observations used, can be found in Section 2, the results in Section 3 and the conclusions and future work in Section 4.

2. Methodology

Figure 1 shows the current method of solar wind modeling in the top flow diagram, with photospheric magnetic field observations initializing the coronal model which then feeds into the heliospheric model. The middle flow diagram shows how BRaVDA is incorporated into the modeling framework, by adding in a further step that updates the inner boundary of the heliospheric model. Finally, the bottom flow diagram shows the elements introduced in this work in the yellow boxes, which includes processing of the BRaVDA output and merging this with the original WSA map. These stages are described in more detail below.

2.1. WSA

The Wang-Sheeley-Arge (WSA) model (C. Arge & Pizzo, 2000; C. N. Arge et al., 2003) is a semi-empirical model of the corona that combines a potential field source surface (PFSS) model (Altschuler & Newkirk, 1969) and the Schatten Current Sheet (SCS) model (Schatten et al., 1969) to estimate the coronal magnetic structure consistent with the observed photospheric magnetic field. An estimate of solar wind speed is then produced using an empirical relation to the coronal magnetic field topology.
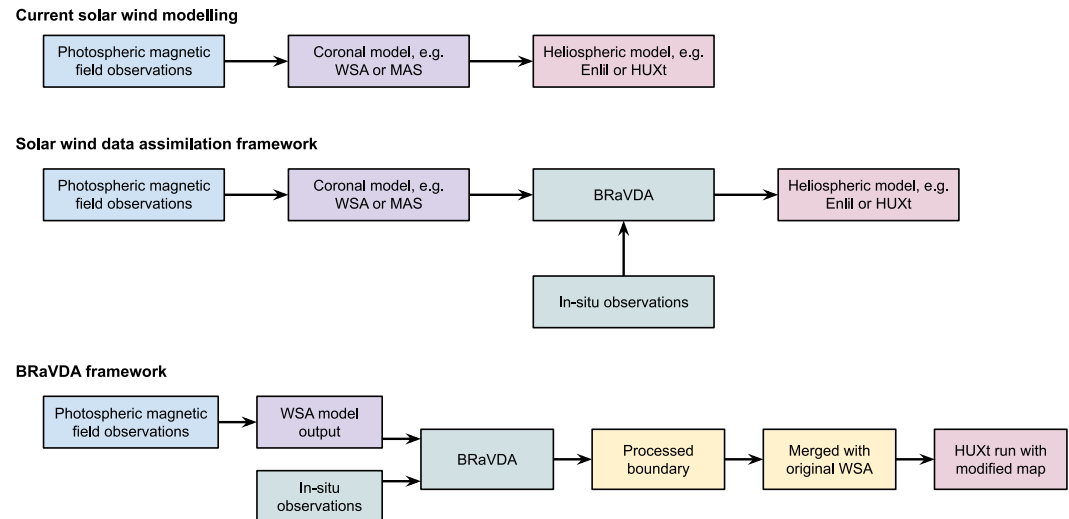
Figure 1. Schematic of the current framework for solar wind modeling (top), how previous experiments with solar wind data assimilation have been carried out (middle) and the alterations to the BRaVDA framework presented in this work (bottom).

Observations of the photospheric magnetic field (magnetograms) are used as input into the PFSS model. As a complete map of the photosphere is required, and observations are only available of the Earth-facing hemisphere, it is necessary to use observations from the previous solar rotation to produce the inner boundary condition. In this study, photospheric observations are provided by the Global Oscillations Network Group (GONG, Harvey et al., 1996), as this is typically used as the basis for operational forecasting. The PFSS model has its inner boundary at the photosphere, where the magnetograms are used to define the inner boundary condition of the radial magnetic field. The outer PFSS boundary is known as the "source surface," which is the point where all the field is again required to be radial. Thus any magnetic loops which have their apex below the source surface height are closed, and will not contribute to the heliospheric magnetic field. Typically, the source surface is set at a radial distance of 2.5–3.25 rS (Riley et al., 2006).

The output from the PFSS model is used in the SCS model, which gives a more realistic representation of the magnetic field in the upper corona. At the outer boundary to the SCS model, typically at 21.5 rS, the field is again radial. But within the SCS domain, the magnetic flux can expand non-radially so that $|B_R|$ is approximately equal over the outer boundary, as inferred from in situ observations (Lockwood et al., 2004; E. J. Smith & Balogh, 1995). In order to reduce the discontinuity at the PFSS/SCS interface, the magnetic fields of the two models are matched across the boundary to reduce kinks present in the field lines (McGregor et al., 2008).

Once the magnetic field configuration has been obtained, it is next necessary to infer the associated solar wind speed. Two properties of the magnetic field topology are typically used; the degree of expansion of magnetic flux tubes between the photosphere at 21.5 rS, and the distance of the magnetic field footpoint to the nearest open/closed field boundary on the photosphere. These two properties are used with an empirical relationship to estimate the solar wind speed at 5 rS (C. N. Arge et al., 2003). The solar wind is then accelerated out to 1 AU using a simple kinematic propagation. This means that the WSA speeds will be too high for use at 21.5 rS and require deaccelerating before being used as an inner boundary for a solar wind model. In the work here, we deaccelerate the WSA speeds from 1 AU to 21.5 rS (0.1 AU), typically of the order 20%.

The magnetic field and speeds at 21.5 rS then need to be propagated to Earth in order to provide a forecast. Two approaches have been taken. In the original formula of the WSA model, a simple kinematic approach is used to propagate the solar wind out to Earth's orbital radius (1 AU), allowing for stream interactions (C. Arge & Pizzo, 2000). As there is no net acceleration between 0.1 and 1 AU, the empirical relation between magnetic topology and solar wind speed is tuned to match observed solar wind speeds at 1 AU. More recently, WSA has been used to provide the inner boundary conditions to numerical magnetohydrodynamic (MHD) heliospheric models, such as Enlil (Odstrcil, 2003) and EUFHORIA (Pomoell & Poedts, 2018). As such heliospheric models produce a net acceleration of the solar wind between 0.1 and 1 AU, typically of the order 20%, it is necessary to

scale and clip the WSA solar wind speeds between upper and lower limits, for use at the inner boundary (often $21.5R_S$) of the heliospheric model. This is often done in a fairly ad-hoc manner and tends not to be very well documented in the literature (with some notable exceptions that touch on the relevant ambient wind parameters for Enlil, including Falkenberg et al. (2010), Jian et al. (2011), Wold et al. (2018), Mays et al. (2015, 2020)).

2.2. BRaVDA

The Burger Radius Variational Data Assimilation (BRaVDA) scheme is a 4D-variational DA scheme. The full methodology is described in Lang and Owens (2019), hence we only provide a short description here.

The output from a coronal model is used (here, WSA) as the input into BRaVDA, alongside in situ observations of the solar wind speed. As BRaVDA is run on a single latitudinal plane, only the WSA values from the required latitude are used. The assimilation window for BRaVDA is 27-day long, corresponding to the solar synodic period, when similar solar wind states are likely to reoccur (e.g., Kohutova et al., 2016; M. J. Owens et al., 2013). Therefore, observations from the 27-day prior to the forecast date will be assimilated. The aim is to find the solar wind state that contains the lowest error contribution from the prior and the observations, whilst taking into account their relative uncertainties. This is achieved by minimizing a cost function through a minimization algorithm, resulting in an estimate of the most probable solar wind speed state given the observations. To use such a system successfully, the model the DA is based upon must be computationally inexpensive, otherwise each run would take too long to be of value. For this reason, the model is the reduced-physics solar wind model "HUX" (Riley & Lionello, 2011) and makes use of in situ spacecraft observations from close to Earth's latitude. HUX neglects magnetic and plasma pressure forces, and assumes a steady-state solar wind.

Once an optimal state is found, we now have an inner boundary condition that contains information from the in situ observations and should be more representative of the true state. BRaVDA is run in 2-dimensions at a single latitude, typically the helio-equator or Earth's heliographic latitude. In previous studies (Turner et al., 2022, 2023), observations from multiple spacecraft at similar heliolatitudes, such as the STEREO spacecraft and Wind or ACE at L1 (see Section 2.2.1), have been used in a single BRaVDA solution. This implicitly assumes all observations are at the same heliolatitude. In reality, the inclination of the ecliptic place to the helioequator means that they can differ by up to 14°, which can result in significantly different solar wind being observed (Chakraborty et al., 2023; M. J. Owens, Lang, Barnard, et al., 2020; Turner et al., 2021), and hence error in the reconstruction of the solar wind at the inner boundary. An alternative way to treat this problem is to perform multiple independent BRaVDA solutions, each assimilating in situ data from only one spacecraft. This results in multiple inner boundary solutions, each at the latitude of each spacecraft.

For updated boundary conditions to be used in a 3-dimensional solar wind model, conditions at a single latitude are insufficient. It is necessary to merge the original global WSA map with the BRaVDA solutions at discrete latitudes in order to provide full coverage at the inner boundary. This can be achieved by merging the update over a range of latitudes, centered around the latitude of the observing spacecraft, as discussed further below.

2.2.1. Data

In this study, we use in situ solar wind observations from the Solar Terrestrial Relations Observatory (STEREO) spacecraft and the OMNI data set. These data are chosen as they provide near-continuous observations of the solar wind close to the heliographic equator. They also move slowly in heliographic latitude, meaning the assumption of constant latitude over a 27-day assimilation window is reasonable.

The STEREO mission is a twin spacecraft mission consisting of an Ahead and Behind spacecraft (STEREO-A and STEREO-B respectively, Kaiser et al., 2008). These were launched in 2007 on Earth-like orbits, separating in longitude from Earth at a rate of approximately 11° per year. They passed behind the Sun in 2014, and contact with STEREO-B was lost, resulting in only STEREO-A data being available for this study. During the period of study used here, 2020, the STEREO-A spacecraft moved from −78.5° longitude in Heliocentric Earth Ecliptic (HEE) coordinates to −56.8°, and reached a maximum of 9.1° latitudinal separation from Earth. In this study, science level data from the Plasma and Suprathermal Ion Composition (PLASTIC, Galvin et al., 2008) instrument is used. This instrument infers the in situ solar wind speed by measuring the particle flux at certain energy levels through a range of potential differences.

The OMNI data set is a product produced from a succession of spacecraft, such as ACE and Wind, at the L1 point. The data is intercalibrated and ballistically propagated to the bow shock of Earth (Vokhmyanin et al., 2019). This data set proves very useful for near-Earth solar wind exploratory research studies, as it circumvents the complexities encountered with near-real time solar wind observations, which must unavoidably be tackled at later stages of the research-to-operations process (e.g., Beggan et al., 2025; Loto'aniu et al., 2022; A. Smith et al., 2022).

Previous work has shown that assimilating observations containing CMEs can introduce false fast streams into the forecasts, owing to BRaVDA "assuming" that any increase in solar wind speed is due to a stream of fast wind, rather than a transient event (Turner et al., 2022). Therefore, for the work here, CMEs are removed from the observations used in the assimilation process and the observations used in the verification.

2.3. HUXt

The Heliospheric Upwind Extrapolation with time-dependence (HUXt) model is a reduced physics model that fills the gap between a ballistic approach and the full MHD approach (Barnard & Owens, 2022; M. Owens, Lang, Barnard, et al., 2020). As the name suggests, it is based on the HUX model, but relaxes the steady-state assumption, allowing time-dependent structures such as CMEs to be modeled. In summary, HUXt neglects magnetic and plasma pressure and treats the solar wind as a 1-dimensional inviscid and incompressible flow. An upwind scheme is used to propagate a velocity stream from the inner boundary out into the heliosphere in radial steps, with an empirically set acceleration term that accounts for residual acceleration out through the heliosphere (M. Owens, Lang, Barnard, et al., 2020). Despite these approximations, HUXt reproduces the flow fields from a numerical 3D MHD model to within about 5% (M. Owens, Lang, Barnard, et al., 2020), but with a vastly reduced computation time, allowing the efficient use of large ensembles.

Previous testing of BRaVDA at a daily cadence has made use of the HUX (not HUXt) model, to propagate the updated inner boundary out to 1 AU. As the HUXt model is time-dependent, this allows for CMEs to be inserted at the inner boundary and provides results closer to those of an MHD model. Given that HUX and dynamical model (such as HUXt) solutions can differ, it is necessary to test and calibrate BRaVDA output for use with time-dependent heliospheric models.

2.4. Experimental Setup

To test and tune BRaVDA output for use with HUXt, we use an archive of WSA solutions from 2020. The version of WSA used here is 5.4 and this is initialized using GONGz magnetograms, which are a daily updated map product that is zero point uncertainty corrected (Harvey et al., 1996; Hill, 2018). WSA data can be found at https://iswa.ccmc.gsfc.nasa.gov/iswa_data_tree/model/solar/. Data is available for 314 days out of 366 in 2020 and, where the data is available, experiments are run on a daily cadence. To produce time series of a specific lead time, data is taken in 24-hr chunks at that lead time from each daily run to form a contiguous time series.

Figure 2 shows an example of an assimilation window and a forecast window, comparing the runs from WSA-HUXt (black), WSA-BRaVDA (using HUX, blue) and WSA-BRaVDA-HUXt (red). To address the discrepancies in the HUX/HUXt output highlighted in Figure 2, two methods of processing are applied to the BRaVDA output in order to be used as input to HUXt. Firstly, the difference in the way the acceleration profile is solved means that a reduction needs to be applied to prevent a HUXt overestimation at Earth. This has been applied as a simple percentage reduction, reducing all speeds by a set fraction. The magnitude of this reduction is a free parameter that will be determined in Section 3.1. In addition to this, a small shift in longitude is applied, the size of which depends on the magnitude of the reduction. As the speeds are reduced at the inner boundary, this means that any high speed stream will take longer to reach 1 AU and this introduces a timing error. Therefore, the timing difference between the original and the reduced speeds is calculated, and this corresponds to a shift in longitude. For a reduction of 10%, this shift is approximately 9° for an average solar wind speed of 400 km/s.

Secondly, BRaVDA introduces smaller-scale structure into the inner boundary due to there being many available solutions at 0.1 AU to reproduce the time series at 1 AU. With the HUX numerical scheme used internally by BRaVDA, this structure is smoothed out by 1 AU, so the inner boundary conditions are degenerate in terms of matching near-Earth observations. But with the HUXt numerical scheme, this structure is maintained to Earth and is found to be inconsistent with observations. To address this, a smoothing factor is required at the inner boundary
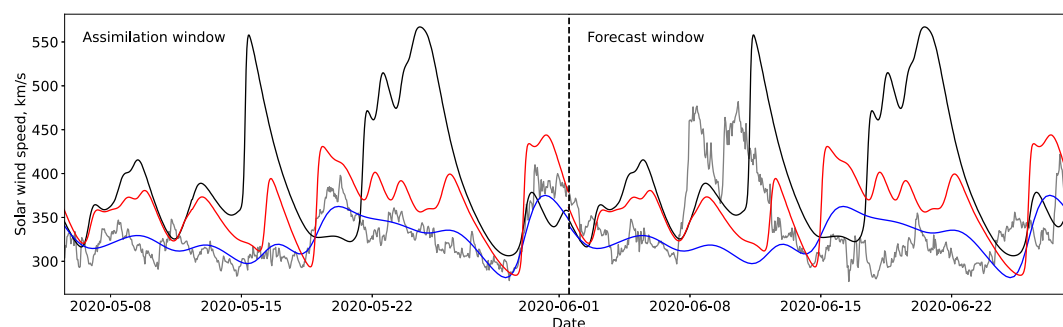
Figure 2. Example time series of an assimilation window and a forecast window, with forecast date of 01/06/2020 (vertical black dashed line). The OMNI observations are shown in gray. The WSA solution is taken from the forecast time and the previous 27-day (assimilation window) of OMNI observations are assimilated. The inner boundary is run forwards for 27-day in the forecast window. The black line shows the WSA solution run with HUXt only, the blue line shows the altered WSA inner boundary condition from the BRaVDA run with HUX (built-in solar wind model) and the red line shows the same boundary condition but run with HUXt.

to reduce the introduction of too much structure into the solar wind state at Earth. This is achieved by using a Gaussian filter, which retains more of the sharp rises in solar wind speed from rotating fast streams than when using a uniform filter. The Gaussian filter calculates a weighted average on each value, with the number of values averaged over depending on the width of the Gaussian. The width can be varied by adjusting the standard deviation of the distribution and the optimum value is determined in Section 3.1.

Following these BRaVDA processing steps, we then seek to generate a new set of inner boundary conditions for 3D solar wind models. This necessitates determining the latitudinal range over which the BRaVDA update should be applied, and how it should be weighted relative to the WSA speed estimates. This is discussed in Section 3.2.

Throughout, we make the distinction between a solar wind "reconstruction" and a solar wind "forecast" (technically a hindcast, but the term "forecast" is used for simplicity). To reconstruct the solar wind, we use the updated inner boundary condition from BRaVDA and use it with HUXt to model the solar wind over the 27-day BRaVDA assimilation window. To forecast the solar wind, we use the updated inner boundary with HUXt to project forwards into the future, 27 days from the last solar wind observation, which is how the DA would be used operationally.

3. Results and Discussion

3.1. Processing Input for Use in HUXt

Figure 3 shows the impact of the different processing methods on the inner boundary that is put into HUXt. All panels show the prior in black, which contains some very sharp rises to speeds of 400–500 km/s and smaller scale, "spiky" features. The posteriors are shown in red, with the unmodified posterior in panel a, optimum smoothing in b, optimum reduction in c and both the optimum smoothing and reduction combined in d. In this case, from 01/06/2020, the DA has reduced the speed of the fast streams located between 200 and 270° in Carrington longitude and at 340°, whilst increasing the solar wind speed between these streams. Smoothing the input removes a lot of the smaller-scale structure, yet retains the larger-scale features.

The first experiments seek to determine the percentage reduction to BRaVDA solar wind speed for optimum use as input with the HUXt model. Figure 4a shows the mean-absolute error (MAE) between the HUXt solar wind speed at Earth and the OMNI observations at 1-hr resolution during the assimilation window, as a function of BRaVDA speed reduction applied to the HUXt inner boundary. A reduction of 10% of the input speed is optimal in reproducing the solar wind speed at Earth.

The second set of experiments seek to determine the optimum level of smoothing for the BRaVDA speeds for use as input to HUXt. A Gaussian filter is used at each of the 128 longitude points. A value of 0 standard deviation represents the unmodified BRaVDA solar wind speeds at 0.1 AU. Varying the standard deviation and calculating the MAE between the reconstructed solar wind in the assimilation window and observations, allows the optimum
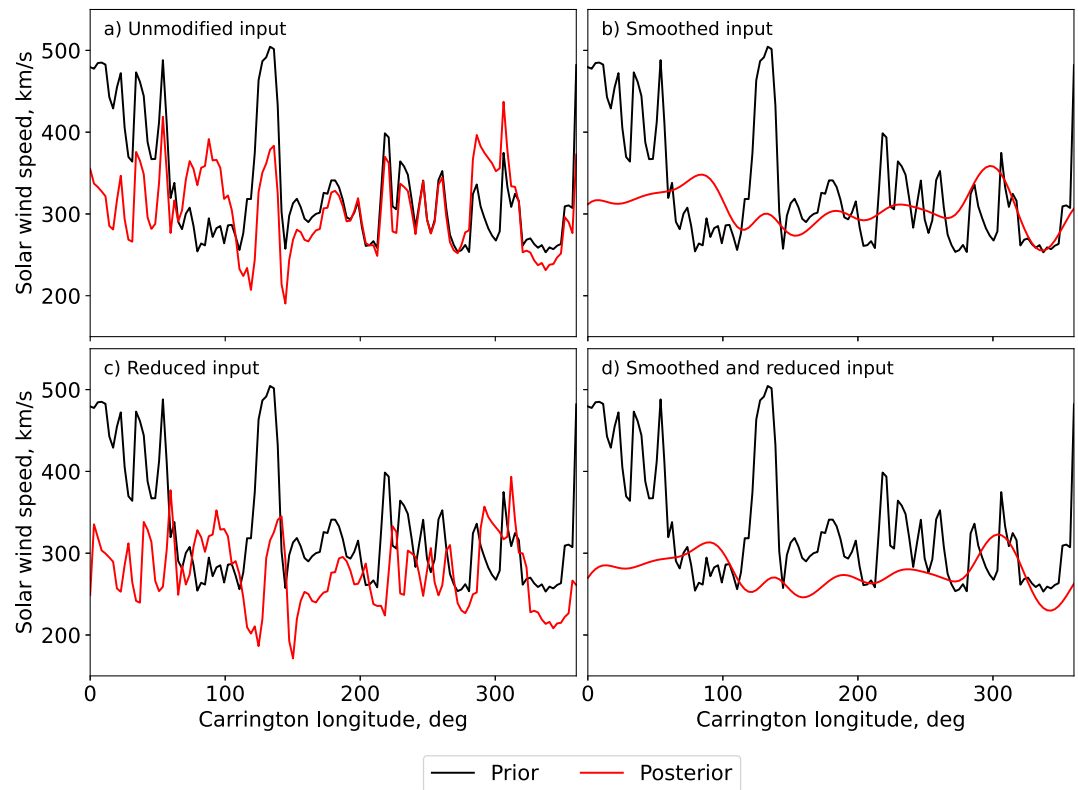
Figure 3. Example of the input into HUXt for 01/06/2020, illustrating the impact of the different processing techniques on the posterior. In all panels, the black line shows the prior. Top left: unmodified prior in red, top right: smoothed posterior in red with Gaussian standard deviation of 4, bottom left: posterior reduced by 10% in red, bottom right: smoothed and reduced posterior in red with Gaussian standard deviation of 4 and reduced by 10%. Here, we are not attempting to match the posterior to the prior.
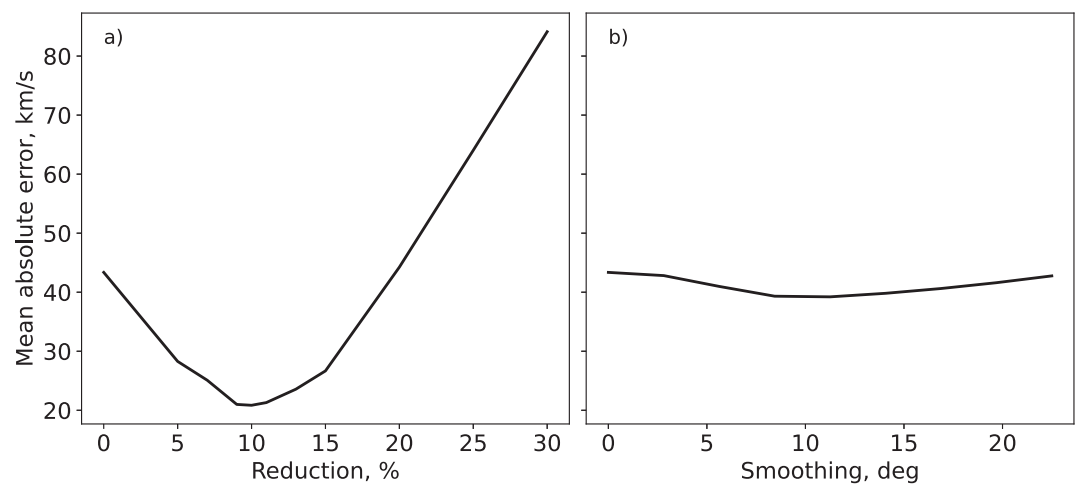

Figure 4. Variation of the mean absolute error (MAE) between reconstructed and observed solar wind speed at Earth, (a) with the percentage reduction of the BRaVDA solar wind speeds at the HUXt inner boundary and (b) with the level of smoothing of the BRaVDA solar wind speeds at the HUXt inner boundary. Reduction of the BRaVDA speeds is achieved by applying a percentage decrease. Smoothing is achieved using a Gaussian filter, which computes a weighted mean. The level of smoothing is changed by varying the standard deviation of the Gaussian, corresponding to the number of points being averaged over. Each increase in standard deviation corresponds to approximately 2.9° in longitude. Here, 0 standard deviation refers to the input with no smoothing. The analysis period spans the whole of 2020.
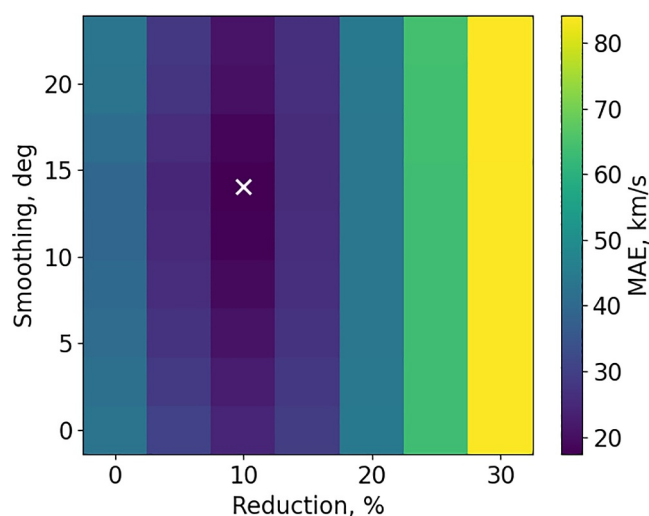
Figure 5. 2-dimensional mean absolute error (MAE) matrix plot of all combinations of reduction and smoothing of the HUXt input, for 0%–30% and 0–23.2° respectively. The minimum MAE (white cross) is found with a 10% reduction and in the range from 5 to 15° width in the Gaussian filter responsible for the smoothing.

width of the Gaussian to be found. As shown in Figure 4b, the minimum MAE is found with a standard deviation of 11.4° in longitude.

Both of these experiments consider the speed reduction and smoothing in isolation. However, smoothing will also modify the speed extremes, so there is the potential for confounding interplay between these two processing aspects. To find the optimum combination of smoothing and reduction, experiments were run with all possible combinations of Gaussian smoothing and percentage speed reduction. Figure 5 shows a 2-dimensional matrix plot of the experiments. The minimum MAE is found with a 10% reduction and the Gaussian standard deviation in the range 5.8–14.5°. The vertical bands are due to the relatively small dependence of MAE on smoothing relative to speed reduction. This highlights that a systematic bias in speed results in a greater MAE than small-scale fluctuations about the correct value. Given that Figure 4b also finds the optimum standard deviation at 11.4°, we can conclude that there is little interaction between the reduction and the smoothing and the previous values can be used in conjunction with each other.

Using the series in Figure 3 as input to the HUXt model, results in the near-Earth solar wind reconstructions can be seen in Figure 6. The posterior time series are in red and organized in the same manner as Figure 3. The fast structures at the inner boundary in the prior state are propagated outwards and result in solar wind streams (black line Figure 6a) more than 200 km/s too high when compared to the observations (gray, all panels). As Table 1 shows, the unmodified posterior (red line in Figure 6a) performs significantly better than the prior, largely due to the reduction of the amplitude of the fast streams. Smoothing the posterior (Figure 6b) helps to reduce the effect of the small scale structure, but has less of an impact on the MAE than applying the 10% reduction (Figure 6c). Combining the two (Figure 6d) produces the lowest MAE and it visually fits the observations much better.

Using the updated boundary condition to initialize a forecast, we can assess the effect of the processing on forecast performance at varying lead times over the whole analysis period, with 0-day lead time corresponding to the date of the last assimilated observation. Figure 7a shows the variation of MAE for lead times of up to 27-day in 2020, with the prior in black, and the different posteriors in the colored lines. The prior forecast shows a sharp rise in MAE at lead times of 7–10 days, before returning to lower values beyond 11 days. The reason for this is unknown; however, as Figure 8 shows, the WSA forecasted speeds are anomalously high for the first 4 months of the year. This is for a lead time of 5-day, but this general over-prediction is present in time series for other lead times as well (not shown). Both the unmodified and the processed posteriors show an almost factor two improvement over the prior, especially during the period where the speeds are too high. This shows that the DA is working well to correct the bias in the prior, which could prove useful during future times when such a bias is present. Further to this, the smoothed and reduced posterior forecasts produce an MAE that is approximately a further 20 km/s lower than the unmodified posterior (Figure 7). It can also be seen in Figure 8 that smoothing and reducing the input reduces the jump between each day in the stitched-together forecast time series. Therefore, the time series is more continuous between days.

The 2020 period was in solar minimum and had a largely flat heliospheric current sheet throughout the year. We expect that the processing of the BRaVDA output should not be dependent on the solar cycle. As a test, we apply the same processing parameters for the reduction and smoothing to forecasts in 2014, in the maximum of cycle 24. As Figure 7b shows, the reduction and smoothing parameters have a comparable impact on the forecast MAE as during the solar minimum period. Therefore, the optimum parameters found here are expected to be applicable across all phases of the solar cycle.

3.2. Generating Modified WSA Maps

In order to generate a full set of updated boundary conditions at 0.1 AU, it is necessary to merge a WSA map with the BRaVDA posterior. Ideally, the BRaVDA estimates of solar wind speed at 0.1 AU would be assimilated into the coronal model to produce a new global coronal solution in a fully self-consistent way. However, this capability does not exist and would be extremely challenging to implement. Instead, we take a pragmatic approach and blend
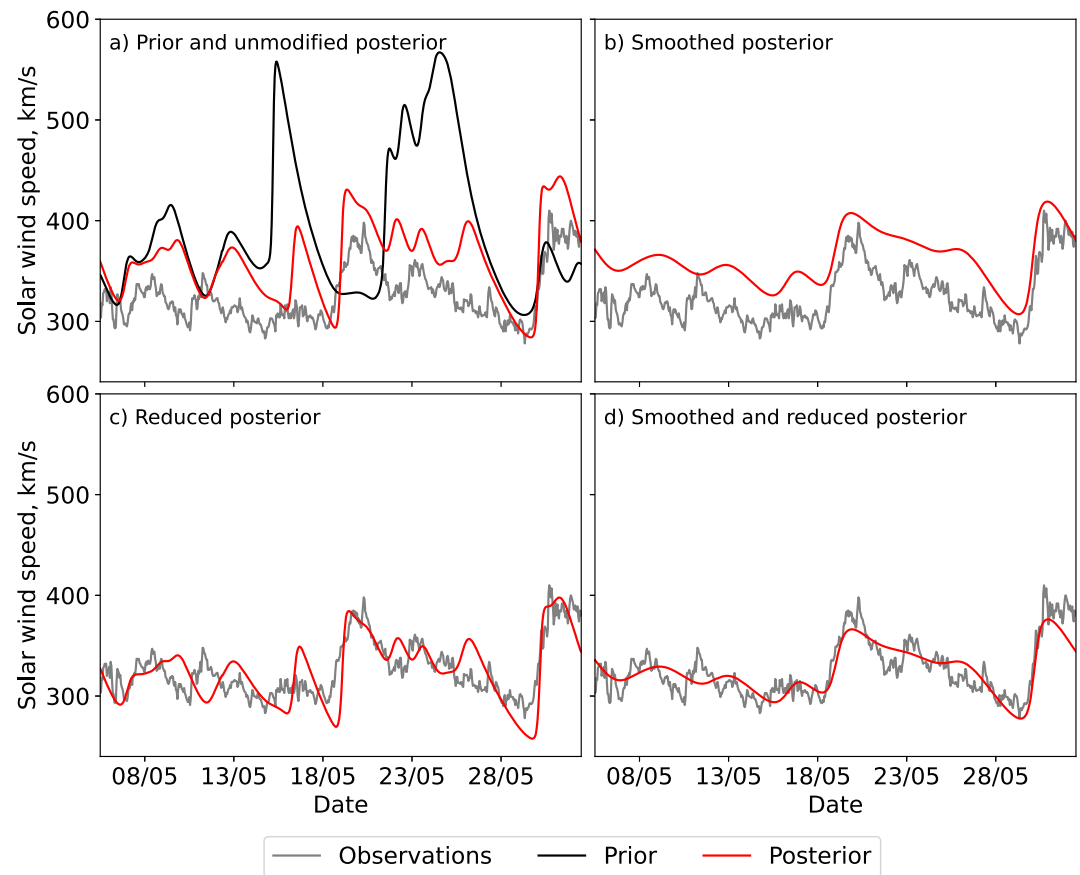
Figure 6. Example of time series at Earth for the different inputs into HUXt on 01/06/2020. In all panels, the gray line shows the observations taken from the OMNI data set for near-Earth. Panel (a) prior in black and unmodified posterior in red, panel (b) smoothed posterior in red with Gaussian standard deviation of 4 grid steps (11.4°), panel (c) posterior reduced by 10% in red, panel (d) smoothed and reduced posterior in red with Gaussian standard deviation of 4 and reduced by 10%. The average mean absolute errors across the time window are in Table 1.

the global WSA solution and the spatially-limited BRaVDA solution. As the BRaVDA posterior only applies at the latitude of the assimilated spacecraft, we must determine the latitude range over which the BRaVDA posterior should have a higher influence than the WSA values. If the spread of latitude over which BRaVDA is prioritized is too low, then the update will have a limited impact on the solar wind state away from this latitude. If the spread is too high, then too much equatorial wind will be spread up to higher latitudes, which will not be physical and will introduce further error into a forecast. This spread can be achieved by using a Gaussian weighting of the posterior centered on the observation (typically Earth) latitude, and the width of this distribution determines the overall latitudinal spread of the update. Figure 9 shows an example of an original WSA map that has been deaccelerated to 21.5 rS from 01/06/2020 in panel a, the posterior is applied with a 2° spread in panel b, 4° spread in panel c and 6° spread in panel d.

The speed at a given latitude is calculated as some weighting of the WSA solution combined with a weighting of the posterior. When two spacecraft sources are used, each posterior has its own Gaussian weighting and the WSA weighting is not allowed to go below zero. The calculation of the posterior weighting and therefore the solar wind speed at a given latitude can be seen below.

For a single spacecraft;

$$V = W_A \cdot V_A + (1 - W_A) \cdot V_{WSA} \tag{1}$$

Table 1

Average Mean Absolute Error (MAE) for the Solar Wind Speed Reconstruction at Earth for the Period 01/06/2020 to 28/06/2020 for the Different Processing to the HUXt Input

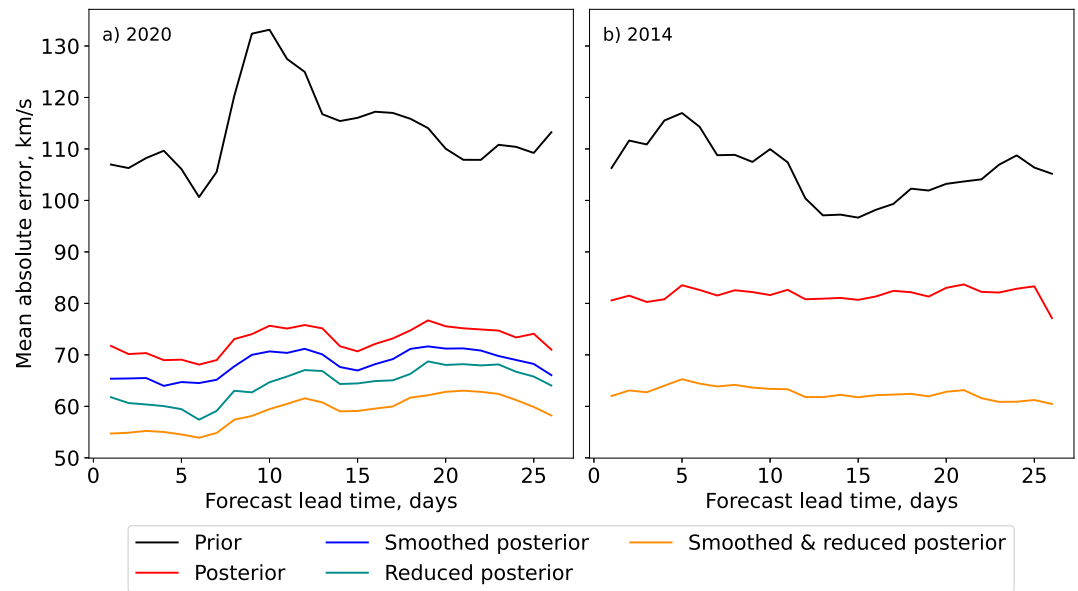| Reconstruction	MAE (km/s)
Prior	76.0
Unmodified posterior	37.3
Smoothed posterior	35.5
Reduced posterior	17.5
Smoothed and reduced posterior	11.6

Figure 7. Variation of forecast mean absolute error (MAE) with the forecast lead time for daily initialized forecasts using different processing of the input to HUXt. Panel (a) shows the analysis of 2020 (solar minimum) and panel (b) shows the analysis of 2014 (solar maximum). The prior is shown in black, unmodified posterior in red, smoothed posterior in blue (Gaussian standard deviation of 4), reduced posterior in teal (reduced by 10%) and the smoothed and reduced posterior in orange (Gaussian standard deviation of 4 and reduction of 10%).
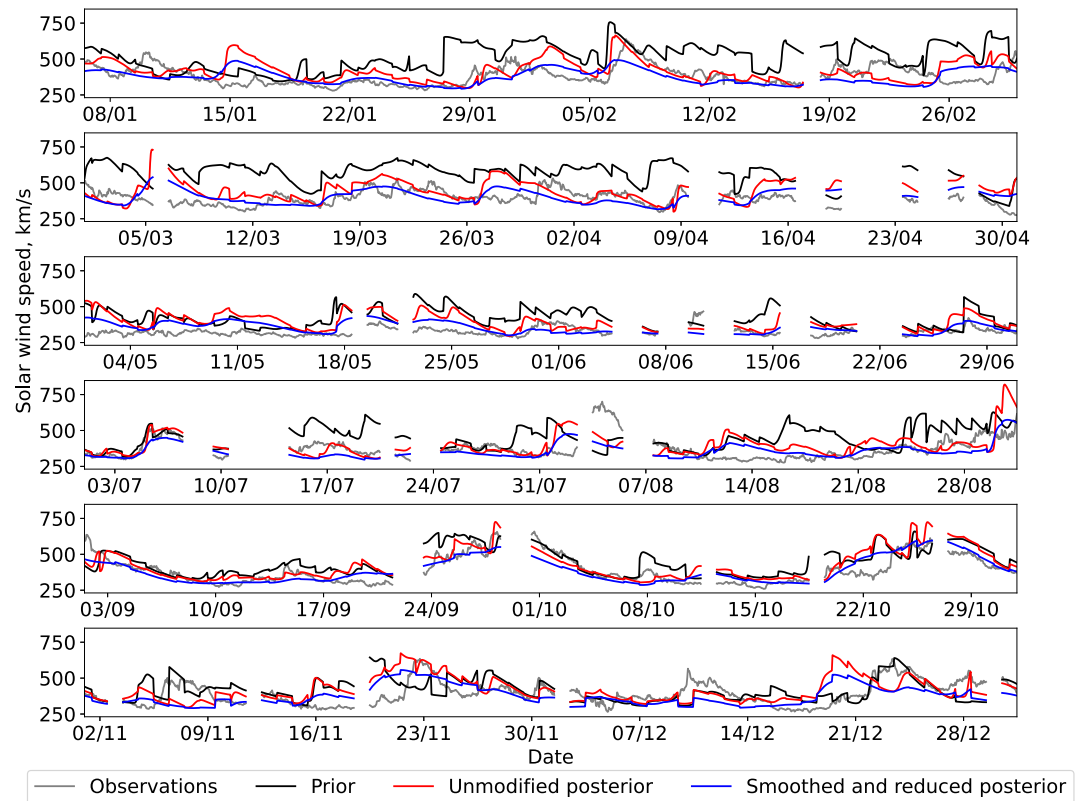

Figure 8. Forecast time series for 2020, with a 5-day forecast lead time. The prior is shown in black, unmodified posterior in red and smoothed and reduced posterior (Gaussian standard deviation of 4 and reduced by 10%) in blue. The observations from the ACE spacecraft at L1 are in gray.
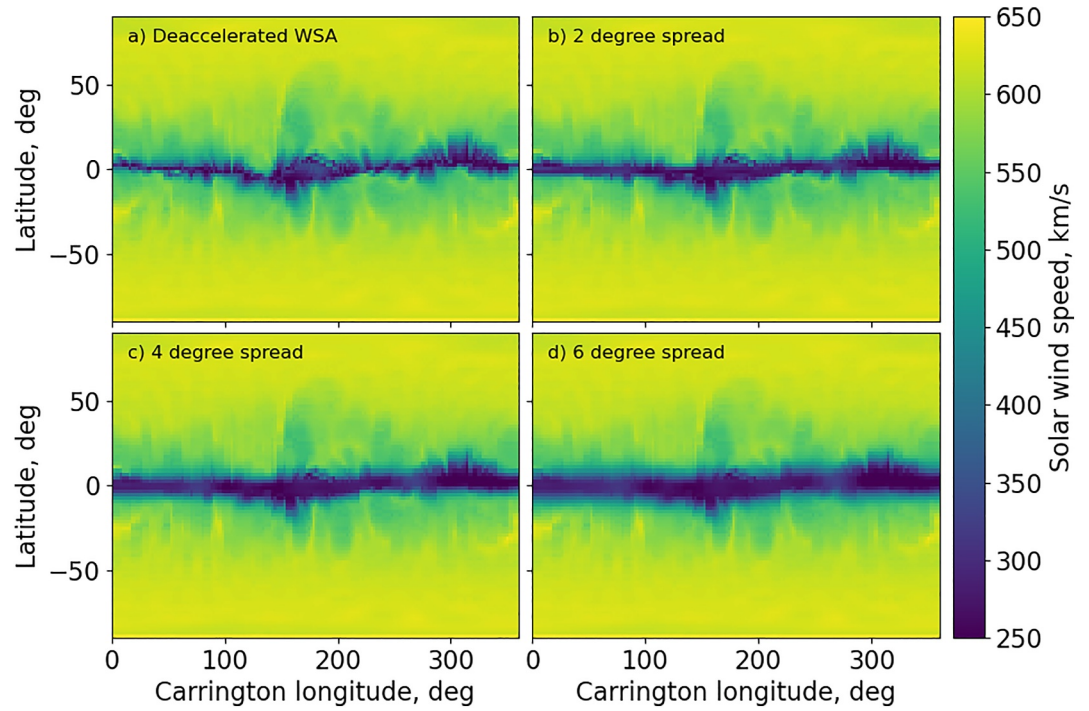
Figure 9. Example of a WSA map for 01/06/2020 that has no update from the data assimilation in panel (a), an update spread over 2° in panel (b), 4° in the panel (c) and 6° in panel (d).

where V = solar wind speed, W_A = spacecraft weighting for observer A, V_A = speed from the BRaVDA posterior for observer A and V_{WSA} = speed from the WSA solution.

For multiple spacecraft;

The weighting for WSA is calculated such that;

$$W_{WSA} = 1 - W_A - W_B \qquad (2)$$

where W_{WSA} = weighting for WSA, W_A = weighting for observer A and W_B = weighting for observer B.

To account for when $W_A + W_B > 1$, we do not allow the WSA weighting to be less than 0;

$$\text{when } W_{WSA} < 0, \text{ set } W_{WSA} = 0 \qquad (3)$$

Therefore, the solar wind speed at any given latitude (V) is given by;

$$V = \frac{W_{WSA} \cdot V_{WSA} + W_A \cdot V_A + W_B \cdot V_B}{W_{WSA} + W_A + W_B} \qquad (4)$$

where V_{WSA} = speed from the WSA map, V_A = speed from the BRaVDA posterior for observer A and V_B = speed from the BRaVDA posterior for observer B.

Turner et al. (2021) has shown that beyond a latitudinal separation of 5° between the spacecraft providing the observations and the location of the forecast, there is an increasing error contribution from the latitudinal separation. Therefore, we limit the influence of the observations, that is the spread of the posterior, to close to 5° around the latitude at which the update is applied. For a Gaussian with a width of 4°, this ensures that at 5°, the posterior has a weighting approximately 0.5. The left hand panel of Figure 10 shows the weighting for a single update being applied at a latitude of approximately 0°. The black line shows the weighting of the background WSA map and the red line shows the weighting of the update from assimilating only the OMNI observations.
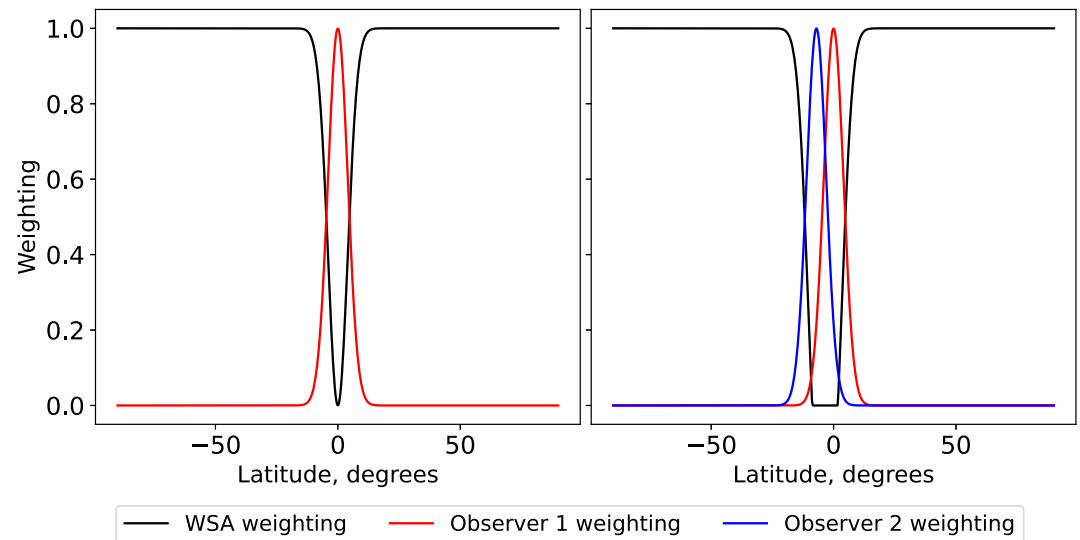
Figure 10. Example of how the WSA map and the BRaVDA posterior are weighted in latitude using a Gaussian of width 4°. The left hand panel shows a single update applied by assimilating near-Earth data when the heliographic latitude was 0°, with the weighting to the background WSA map in black and the weighting to the BRaVDA posterior in red. The right hand panel shows the weighting when two sources of observations are assimilated. Observer 1 (red) is located at 0° latitude and Observer 2 (blue) is located at −7° latitude. The WSA weighting is reduced to 0 when the total observer weighting exceeds 1 in the crossover region between the two Gaussians.

When more than one observation source is assimilated, multiple updates can be applied to the map at their respective latitudes, each with an individual weighting. The sum of the weightings can exceed 1, so to ensure that the weighting of the WSA map does not go below zero, it gets set to zero when the total weighting is greater than 1, as in Equation 3. If this step is not included, WSA will have a negative contribution and will modulate the posterior speeds unnecessarily. The speed at any given latitude is normalized by the total weighting, that is the sum of the WSA weighting and observer weightings, as in Equation 4. For the example in Figure 10, STEREO-A is located at approximately −7° latitude and Earth is located at 0°. Each update has a Gaussian that reaches a maximum value of 1. In the region where the two Gaussians overlap, the WSA weighting is reduced to 0 due to the sum of the observer weightings being greater than 1.

Figure 11 shows the same deaccelerated WSA map from Figure 9 in the left top panel, with only OMNI assimilated in the middle panel and with both OMNI and STEREO-A assimilated in the right hand panel. The bottom row shows the difference between the DA modified map and the deaccelerated map, to highlight where the update is being applied. In all instances, each Gaussian is spread over 4° in latitude.

To assess the effectiveness of the update on the WSA map, we can use observations from the STEREO-A spacecraft to compare with the model output. A full study into the improvement offered by using the BRaVDA output in this way is left for a future study, rather here we show a single forecast window to demonstrate its impact. Figure 12 shows a forecast time series at STEREO-A for a forecast date of 01/11/2020. During this time, Earth and STEREO-A are located approximately 3° apart in latitude and it can be seen that the updated WSA maps, for both sets of assimilation, fit the observations (gray line) more closely. In this time period, the deaccelerated WSA (red line) has an MAE of 114.0 km/s, the WSA map modified with L1 assimilation (blue line) has an MAE of 45.6 km/s and the map modified with both L1 and STEREO-A (black line) has an MAE of 43.3 km/s. This demonstrates that modifying the WSA maps in this way could prove useful for solar wind forecasting, but further study is needing to assess its full impact.

4. Conclusions and Future Work

Knowledge of the solar wind conditions in near-Earth space is essential for accurate space weather forecasting. The current state-of-the-art forecasting system is to use a model of the solar corona, initialized with observations of the photospheric magnetic field, coupled with a model that propagates the solar wind out into the heliosphere.
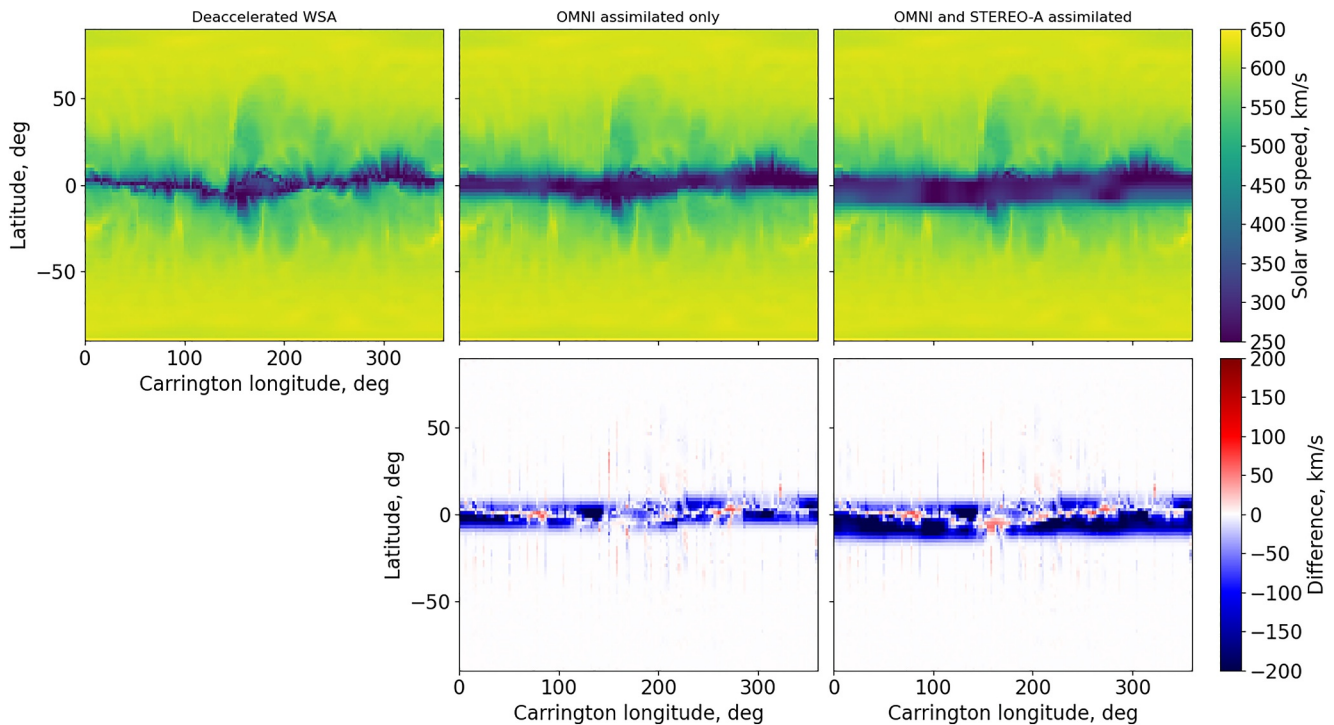
Figure 11. Example of a WSA map from 01/06/2020 that is deaccelerated (left top) but otherwise unaltered, has an update from a single assimilated observation source (middle top) and with two assimilated sources (right top), as in Figure 10. The single update is applied at a single latitude, in this case at a latitude of 0°. The panel with two assimilated sources has an update at −7° and at 0°. The bottom row shows the difference between the modified WSA map and the deaccelerated WSA map, corresponding with the modified map immediately above it.

Beyond the initial observations, there are no further observational constraints on the system when forecasting the ambient solar wind. Data assimilation (DA) is a method of combining model output with observations to form an optimum estimation of reality. The DA system used here, known as BRaVDA, introduces another step into the modeling system. The output from the coronal model is updated using information from observations taken close to Earth's orbital latitude, so that an improved state is found, which can then be used in any solar wind model.

Depending on the dynamics and acceleration profile of the solar wind model being used, some processing of the BRaVDA output may be necessary to produce optimum results at Earth. Previously, BRaVDA has been applied to the MAS coronal model to reproduce and forecast solar wind speed at Earth. Here, we have run several

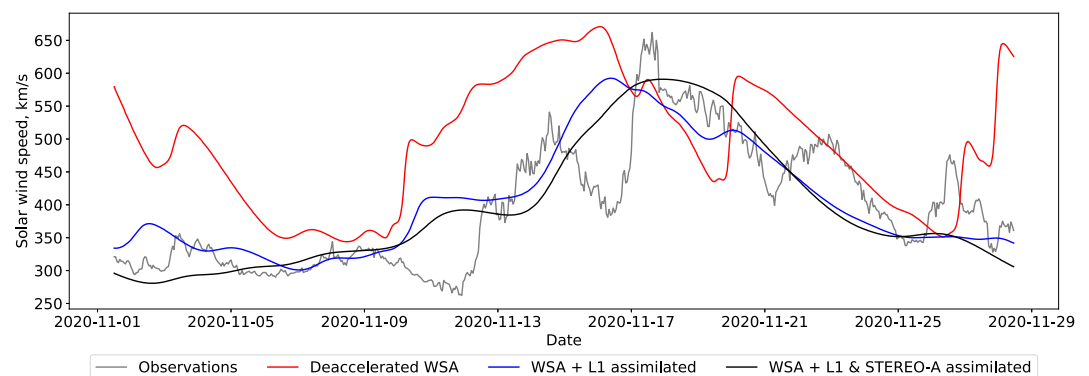**Figure 12.** Forecast time series from the HUXt model at STEREO-A compared with observations (gray), for a forecast date of 01/11/2020. The red line shows HUXt run with the deaccelerated (but otherwise unmodified) WSA, the blue line shows the WSA map updated with the assimilation of L1 observations only and the black line shows the WSA map update with the assimilation of L1 and STEREO-A observations.

experiments using the WSA coronal model, which is more commonly used in an operational context. We also seek to use the output of BRaVDA to provide the inner boundary conditions for a time-dependent solar wind model—in this case, HUXt—to potentially enable improved CME predictions.

To investigate suitable processing methods, we used WSA output from 2020. Without any modification of the BRaVDA output at 0.1 AU, it was found that BRaVDA/HUXt solutions in near-Earth space were biased toward higher speeds and generally contained too much small-scale structure. This is a result of the internal solar wind model used by BRaVDA (HUX) solving the solar wind acceleration profile in a slightly different manner to HUXt and generally being more diffusive to solar wind speed gradients than HUXt. Experiments were run using different levels of speed reduction and smoothing of the BRaVDA conditions at 0.1 AU which serve as the HUXt input. Taking each factor in isolation, it was found that a percentage reduction of 10% of the BRaVDA speeds at 0.1 AU produced the best match to the observed solar wind speeds that were used in the assimilation window. To reduce the small-scale solar wind structure that is preserved to 1 AU in HUXt (but not HUX), we smooth the speed profiles in longitude at 0.1 AU. A Gaussian filter was applied, which performs a weighted average in longitude, the longitudinal width of which can be adjusted by changing the standard deviation of the Gaussian. The optimum standard deviation found was 11.4° in longitude. When investigating the different combinations of smoothing and reduction, it was found that there were no interacting effects and the optimum combination was a 10% reduction and 11.4° smoothing. These parameters were also applicable to the WSA output from 2014, which was during solar maximum. This indicates that there is no solar cycle dependence on the optimum values.

To use the BRaVDA output with a 3-dimensional solar wind model, such as Enlil or EUHFORIA, it is necessary to merge the BRaVDA information at a single latitude with the synoptic information from WSA. To do this, the BRaVDA posterior can be applied using a Gaussian weighting centered on the observations latitude. The width of the Gaussian determines how far the update is spread out in latitude. Previous work has shown that for a spacecraft separation of greater than 5°, there is an increasing error contribution from that separation. Therefore, the width of the Gaussian used to spread the posterior latitudinally is limited to 4°. Initial tests with the HUXt model have shown that modifying the WSA maps in this way could improve solar wind forecasting. Testing the forecast improvement gained from BRaVDA-WSA maps with a 3-dimensional MHD model would be the logical next step for this study. Preliminary experiments conducted are very promising and will be reported in a future study. It is hoped that the use of updated boundary conditions in operational solar wind forecasting models will lead to improvements in solar wind validation metrics for both the ambient wind and CMEs.

Data Availability Statement

An archive of WSA solutions can be found at CCMC (2025). OMNI observations are available at NASA (2025a) and STEREO-A observations are available at NASA (2025b). The BRaVDA code can be found at Lang (2025) and the HUXt code can be found at M. Owens and Barnard (2025).

References

Altschuler, M. D., & Newkirk, G. (1969). Magnetic fields and the structure of the solar corona: I: Methods of calculating coronal fields. *Solar Physics*, *9*, 131–149.

Arge, C., & Pizzo, V. (2000). Improvement in the prediction of solar wind conditions using near-real time solar magnetic field updates. *Journal of Geophysical Research: Space Physics*, *105*(A5), 10465–10479. https://doi.org/10.1029/1999ja000262

Arge, C. N., Odstrcil, D., Pizzo, V. J., & Mayer, L. R. (2003). Improved method for specifying solar wind speed near the sun. In *AIP conference proceedings* (Vol. 679, pp. 190–193). https://doi.org/10.1063/1.1618574

Barnard, L., & Owens, M. (2022). HUXt—An open source, computationally efficient reduced-physics solar wind model, written in python. *Frontiers in Physics*, *10*, 1005621. https://doi.org/10.3389/fphy.2022.1005621

Bauer, P., Thorpe, A., & Brunet, G. (2015). The quiet revolution of numerical weather prediction. *Nature*, *525*(7567), 47–55. https://doi.org/10.1038/nature14956

Beggan, C., Eastwood, J., Eggington, J., Forsyth, C., Freeman, M., Henley, E., et al. (2025). Implementing an operational cloud-based now-and forecasting system for space weather ground effects in the UK. *Space Weather*, *23*(5), e2025SW004364. https://doi.org/10.1029/2025sw004364

Cannon, P. (2013). *Extreme space weather: Impacts on engineered systems and infrastructures*. Royal Academy of Engineering.

Case, A., Spence, H. E., Owens, M., Riley, P., & Odstrcil, D. (2008). Ambient solar wind's effect on ICME transit times. *Geophysical Research Letters*, *35*(15). https://doi.org/10.1029/2008gl034493

CCMC. (2025). Catalogue of WSA solutions. Retrieved from https://iswa.ccmc.gsfc.nasa.gov/iswa_data_tree/model/solar/WSA5.X/R21.5/WSA_OUT/GONG_Z/

Chakraborty, N., Turner, H., Owens, M., & Lang, M. (2023). Causal analysis of influence of the solar cycle and latitudinal solar-wind structure on co-rotation forecasts. *Solar Physics*, *298*(12), 142. https://doi.org/10.1007/s11207-023-02232-4

Eastwood, J., Hapgood, M., Biffis, E., Benedetti, D., Bisi, M., Green, L., et al. (2018). Quantifying the economic value of space weather forecasting for power grids: An exploratory study. *Space Weather*, *16*(12), 2052–2067. https://doi.org/10.1029/2018sw002003

Falkenberg, T. V., Vršnak, B., Taktakishvili, A., Odstrcil, D., MacNeice, P., & Hesse, M. (2010). Investigations of the sensitivity of a coronal mass ejection model (Enlil) to solar input parameters. *Space Weather*, *8*(6). https://doi.org/10.1029/2009sw000555

Galvin, A. B., Kistler, L. M., Popecki, M. A., Farrugia, C. J., Simunac, K. D., Ellis, L., et al. (2008). The plasma and suprathermal ion composition (plastic) investigation on the stereo observatories. *The STEREO Mission*, 437–486. https://doi.org/10.1007/978-0-387-09649-0_15

Gosling, J. T. (1993). The solar flare myth. *Journal of Geophysical Research: Space Physics*, *98*(A11), 18937–18949. https://doi.org/10.1029/93ja01896

Guhathakurta, M. (2021). Everyday space weather. *Journal of Space Weather and Space Climate*, *11*, 36. https://doi.org/10.1051/swsc/2021019

Harrison, R. A., Davies, J. A., Biesecker, D., & Gibbs, M. (2017). The application of heliospheric imaging to space weather operations: Lessons learned from published studies. *Space Weather*, *15*(8), 985–1003. https://doi.org/10.1002/2017sw001633

Harvey, J., Hill, F., Hubbard, R., Kennedy, J., Leibacher, J., Pintar, J., et al. (1996). The global oscillation network group (GONG) project. *Science*, *272*(5266), 1284–1286. https://doi.org/10.1126/science.272.5266.1284

Hill, F. (2018). The global oscillation network group facility—An example of research to operations in space weather. *Space Weather*, *16*(10), 1488–1497. https://doi.org/10.1029/2018sw002001

Jackson, B., Tokumaru, M., Fallows, R., Bisi, M., Fujiki, K., Chashei, I., et al. (2023). Interplanetary scintillation (IPS) analyses during LOFAR campaign mode periods that include the first three Parker Solar Probe close passes of the Sun. *Advances in Space Research*, *72*(12), 5341–5360. https://doi.org/10.1016/j.asr.2022.06.029

Jian, L., Russell, C., Luhmann, J., MacNeice, P., Odstrcil, D., Riley, P., et al. (2011). Comparison of observations at ace and *Ulysses* with Enlil model results: Stream interaction regions during Carrington rotations 2016–2018. *Solar Physics*, *273*(1), 179–203. https://doi.org/10.1007/s11207-011-9858-7

Kaiser, M. L., Kucera, T., Davila, J., St Cyr, O., Guhathakurta, M., & Christian, E. (2008). The stereo mission: An introduction. *Space Science Reviews*, *136*(1–4), 5–16. https://doi.org/10.1007/s11214-007-9277-0

Kalnay, E. (2003). *Atmospheric modeling, data assimilation and predictability*. Cambridge University Press.

Kay, C., Palmerio, E., Riley, P., Mays, M., Nieves-Chinchilla, T., Romano, M., et al. (2024). Updating measures of CME arrival time errors. *Space Weather*, *22*(7), e2024SW003951. https://doi.org/10.1029/2024sw003951

Kieokaew, R., Pinto, R., Samara, E., Tao, C., Indurain, M., Lavraud, B., et al. (2024). Helio1D modeling of temporal variation of solar wind: Interfacing between MULTI-VP and 1D MHD for future operational forecasting at L1. *Journal of Space Weather and Space Climate*, *14*, 19. https://doi.org/10.1051/swsc/2024018

Kohutova, P., Bocquet, F.-X., Henley, E. M., & Owens, M. J. (2016). Improving solar wind persistence forecasts: Removing transient space weather events, and using observations away from the sun-earth line. *Space Weather*, *14*(10), 802–818. https://doi.org/10.1002/2016sw001447

Lang, M. (2025). Bravda code. Retrieved from https://zenodo.org/records/7892408#.ZFJ8o3bMK3A

Lang, M., & Owens, M. J. (2019). A variational approach to data assimilation in the solar wind. *Space Weather*, *17*(1), 59–83. https://doi.org/10.1029/2018sw001857

Lang, M., Witherington, J., Turner, H., Owens, M. J., & Riley, P. (2021). Improving solar wind forecasting using data assimilation. *Space Weather*, *19*(7), e2020SW002698. https://doi.org/10.1029/2020sw002698

Lockwood, M., Forsyth, R., Balogh, A., & McComas, D. (2004). Open solar flux estimates from near-earth measurements of the interplanetary magnetic field: Comparison of the first two perihelion passes of the Ulysses spacecraft. *Annales Geophysicae*, *22*(4), 1395–1405. https://doi.org/10.5194/angeo-22-1395-2004

Loto'aniu, P. T., Romich, K., Rowland, W., Codrescu, S., Biesecker, D., Johnson, J., et al. (2022). Validation of the DSCOVR spacecraft mission space weather solar wind products. *Space Weather*, *20*(10), e2022SW003085. https://doi.org/10.1029/2022sw003085

Mays, M., MacNeice, P., Taktakishvili, A., Wiegand, C., Merka, J., Adamson, E., et al. (2020). *NASA/NOAA MOU annex final report: Evaluating model advancements for predicting CME arrival time*. CCMC.

Mays, M., Taktakishvili, A., Pulkkinen, A., MacNeice, P., Rastätter, L., Odstrcil, D., et al. (2015). Ensemble modeling of CMEs using the WSA–ENLIL+ Cone model. *Solar Physics*, *290*(6), 1775–1814. https://doi.org/10.1007/s11207-015-0692-1

McGregor, S., Hughes, W., Arge, C., & Owens, M. (2008). Analysis of the magnetic field discontinuity at the potential field source surface and Schatten Current Sheet interface in the Wang–Sheeley–Arge model. *Journal of Geophysical Research: Space Physics*, *113*(A8). https://doi.org/10.1029/2007ja012330

NASA. (2025a). OMNI observations. Retrieved from https://omniweb.gsfc.nasa.gov

NASA. (2025b). Stereo-A observations. Retrieved from https://cdaweb.gsfc.nasa.gov

Odstrcil, D. (2003). Modeling 3-D solar wind structure. *Advances in Space Research*, *32*(4), 497–506. https://doi.org/10.1016/s0273-1177(03)00332-6

Opitz, A., Karrer, R., Wurz, P., Galvin, A. B., Bochsler, P., Blush, L., et al. (2009). Temporal evolution of the solar wind bulk velocity at solar minimum by correlating the STEREO A and B plastic measurements. *Solar Physics*, *256*(1–2), 365–377. https://doi.org/10.1007/s11207-008-9304-7

Oughton, E. J., Hapgood, M., Richardson, G. S., Beggan, C. D., Thomson, A. W., Gibbs, M., et al. (2019). A risk assessment framework for the socioeconomic impacts of electricity transmission infrastructure failure due to space weather: An application to the United Kingdom. *Risk Analysis*, *39*(5), 1022–1043. https://doi.org/10.1111/risa.13229

Owens, M., & Barnard, L. (2025). Huxt code. Retrieved from https://zenodo.org/records/12772120

Owens, M., Lang, M., Barnard, L., Riley, P., Ben-Nun, M., Scott, C. J., et al. (2020). A computationally efficient, time-dependent model of the solar wind for use as a surrogate to three-dimensional numerical magnetohydrodynamic simulations. *Solar Physics*, *295*(3), 43. https://doi.org/10.1007/s11207-020-01605-3

Owens, M. J., Challen, R., Methven, J., Henley, E., & Jackson, D. (2013). A 27 day persistence model of near-earth solar wind conditions: A long lead-time forecast and a benchmark for dynamical models. *Space Weather*, *11*(5), 225–236. https://doi.org/10.1002/swe.20040

Owens, M. J., Lang, M., Riley, P., Lockwood, M., & Lawless, A. S. (2020). Quantifying the latitudinal representivity of in situ solar wind observations. *Journal of Space Weather and Space Climate*, *10*, 8. https://doi.org/10.1051/swsc/2020009

Pizzo, V. J. (1982). A three-dimensional model of corotating streams in the solar wind: 3. Magnetohydrodynamic streams. *Journal of Geophysical Research: Space Physics*, *87*(A6), 4374–4394. https://doi.org/10.1029/ja087ia06p04374

Pomoell, J., & Poedts, S. (2018). EUHFORIA: European heliospheric forecasting information asset. *Journal of Space Weather and Space Climate*, *8*, A35. https://doi.org/10.1051/swsc/2018020

Richardson, I. G., & Cane, H. V. (2012). Solar wind drivers of geomagnetic storms during more than four solar cycles. *Journal of Space Weather and Space Climate*, *2*, A01. https://doi.org/10.1051/swsc/2012001

Riley, P., Linker, J., Mikić, Z., Lionello, R., Ledvina, S., & Luhmann, J. (2006). A comparison between global solar magnetohydrodynamic and potential field source surface model results. *The Astrophysical Journal*, *653*(2), 1510–1516. https://doi.org/10.1086/508565

Riley, P., & Lionello, R. (2011). Mapping solar wind streams from the sun to 1 AU: A comparison of techniques. *Solar Physics*, *270*(2), 575–592. https://doi.org/10.1007/s11207-011-9766-x

Riley, P., Mays, M. L., Andries, J., Amerstorfer, T., Biesecker, D., Delouille, V., et al. (2018). Forecasting the arrival time of coronal mass ejections: Analysis of the CCMC CME scoreboard. *Space Weather*, *16*(9), 1245–1260. https://doi.org/10.1029/2018sw001962

Schatten, K. H., Wilcox, J. M., & Ness, N. F. (1969). A model of interplanetary and coronal magnetic fields. *Solar Physics*, *6*(3), 442–455. https://doi.org/10.1007/bf00146478

Schrijver, C. J. (2015). Socio-economic hazards and impacts of space weather: The important range between mild and extreme. *Space Weather*, *13*(9), 524–528. https://doi.org/10.1002/2015sw001252

Schrijver, C. J., Dobbins, R., Murtagh, W., & Petrinec, S. M. (2014). Assessing the impact of space weather on the electric power grid based on insurance claims for industrial electrical equipment. *Space Weather*, *12*(7), 487–498. https://doi.org/10.1002/2014sw001066

Shiota, D., Kataoka, R., Miyoshi, Y., Hara, T., Tao, C., Masunaga, K., et al. (2014). Inner heliosphere MHD modeling system applicable to space weather forecasting for the other planets. *Space Weather*, *12*(4), 187–204. https://doi.org/10.1002/2013sw000989

Smith, A., Forsyth, C., Rae, I., Garton, T., Jackman, C., Bakrania, M., et al. (2022). On the considerations of using near real time data for space weather hazard forecasting. *Space Weather*, *20*(7), e2022SW003098. https://doi.org/10.1029/2022sw003098

Smith, E. J., & Balogh, A. (1995). Ulysses observations of the radial magnetic field. *Geophysical Research Letters*, *22*(23), 3317–3320. https://doi.org/10.1029/95gl02826

Timar, A., Opitz, A., Nemeth, Z., Bebesi, Z., Biro, N., Facskó, G., et al. (2024). 3D pressure-corrected ballistic extrapolation of solar wind speed in the inner heliosphere. *Journal of Space Weather and Space Climate*, *14*, 14. https://doi.org/10.1051/swsc/2024010

Turner, H., Lang, M., Owens, M., Smith, A., Riley, P., Marsh, M., & Gonzi, S. (2023). Solar wind data assimilation in an operational context: Use of near-real-time data and the forecast value of an L5 monitor. *Space Weather*, *21*(5), e2023SW003457. https://doi.org/10.1029/2023sw003457

Turner, H., Owens, M., Lang, M., Gonzi, S., & Riley, P. (2022). Quantifying the effect of ICME removal and observation age for in situ solar wind data assimilation. *Space Weather*, *20*(8), e2022SW003109. https://doi.org/10.1029/2022sw003109

Turner, H., Owens, M. J., Lang, M. S., & Gonzi, S. (2021). The influence of spacecraft latitudinal offset on the accuracy of corotation forecasts. *Space Weather*, *19*(8), e2021SW002802. https://doi.org/10.1029/2021sw002802

Vokhmyanin, M., Stepanov, N., & Sergeev, V. (2019). On the evaluation of data quality in the OMNI interplanetary magnetic field database. *Space Weather*, *17*(3), 476–486. https://doi.org/10.1029/2018sw002113

Wold, A. M., Mays, M. L., Taktakishvili, A., Jian, L. K., Odstrcil, D., & MacNeice, P. (2018). Verification of real-time WSA-ENLIL+ cone simulations of CME arrival-time at the CCMC from 2010 to 2016. *Journal of Space Weather and Space Climate*, *8*, A17. https://doi.org/10.1051/swsc/2018005